Seismometry of radiation-induced quasiparticle bursts in superconducting devices

Francesco Valenti,[1,*,†] Anil Murani,[1,*,‡] Patrick Paluch,[1,2] Robert Gartmann,[3] Lukas Scheller,[3] Richard Weller,[3] Robert Kruk,[4] Thomas Reisinger,[1] Luis Ardila-Perez,[3] and Ioan M. Pop[1,2,5,§]

[1]*IQMT, Karlsruhe Institute of Technology, 76131 Karlsruhe, Germany*
[2]*PHI, Karlsruhe Institute of Technology, 76131 Karlsruhe, Germany*
[3]*IPE, Karlsruhe Institute of Technology, 76131 Karlsruhe, Germany*
[4]*INT, Karlsruhe Institute of Technology, 76131 Karlsruhe, Germany*
[5]*Physics Institute 1, Stuttgart University, 70569 Stuttgart, Germany*

(Received 21 August 2025; revised 16 March 2026; accepted 6 April 2026; published 12 May 2026)

We perform nanosecond-resolution multiplexed readout on six same-chip superconducting microwave resonators. This allows us to pinpoint the position of ionizing radiation impacts on the chip by measuring the differential time-of-flight of the generated phonons, inducing correlated errors in the device, thereby implementing an on-chip seismic array. We correlate the phase response of each resonator—a proxy for the absorbed energy—to the distance from the impact point to uncover a millimetric characteristic length for the phonon-mediated radiation poisoning.

DOI: 10.1103/xmyw-yc9h

I. INTRODUCTION

The quest towards fault-tolerant superconducting quantum computers has recently branched into a multidisciplinary effort between the superconducting quantum electronics and the high-energy physics communities. The reason is that ionizing radiation has been found to have detrimental consequences for quantum applications, as it can lead to reshuffling of the microscopic environment [1] and phonon-mediated quasiparticle poisoning of the superconducting film [2–4]. The latter has been shown to result in correlated errors in both resonators [5,6] and qubits [7–9], undermining the hypothesis of noncorrelated errors for quantum error correction. Despite being partially mitigated by superconducting gap engineering [10–12] and radiation abatement strategies [13], this quasiparticle poisoning poses a challenge to hardware frugal architectures. In particular, it has recently been observed that the logical error per cycle in a quantum processor was limited by high-energy impacts in a one-dimensional repetition code [8], and correlated chip-level errors are still present in the latest error correction demonstration [14]. Understanding radiation-induced, phonon-mediated quasiparticle poisoning in superconducting quantum circuits constitutes an outstanding challenge in the path towards fault-tolerant quantum processors.

In this work, we employ nanosecond-resolution, in-house-developed electronics to perform multiplexed reflection measurements on six same-chip resonators. This allows us to use the arrival time differential for pair-breaking phonons to estimate the on-chip position of the ionizing impact, thereby implementing a superconducting seismic array, in the spirit of Refs. [5,15]. Furthermore, we resolve the fast rise of the resonator response and use it as a proxy for the energy deposited into the resonators. Equipped with these two quantities, we uncover a millimetric characteristic length of correlated errors induced by quasiparticle bursts generated by ionizing impacts. The characteristic length of the generated error-inducing phonon wave front is a mechanical property of the substrate material. It is related to the correlation length of cofiring detectors in the seismic array. The latter further depends on properties of the resonators, the superconducting film, and the coupling to the substrate. In this work we focus on the former.

II. SEISMOMETRY

High-energy particle impacts ("impacts" from now on) on the substrate generate phonons by, e.g., generating electron/hole pairs that recombine, or by displacing nuclei. Phonons impinging on a superconducting resonator with energy above the superconducting spectral gap break Cooper pairs and generate out-of-equilibrium quasiparticles (a so-called quasiparticle burst, and simply "burst" from now on). Typically, in a burst, an energy in the eV-keV range is deposited in the superconducting device [3]. The resulting increase in kinetic inductance lowers the resonant frequency, and the resonator plays the role of a kinetic inductance detector [5,16]. The resonant frequency shift is related to the

*These authors contributed equally to this work.
†Present address: IBM Quantum, IBM T. J. Watson Research Center, Yorktown Heights, 10598 New York, USA.
‡Present address: Alice & Bob, 75015 Paris, France.
§Contact author: ioan.pop@kit.edu

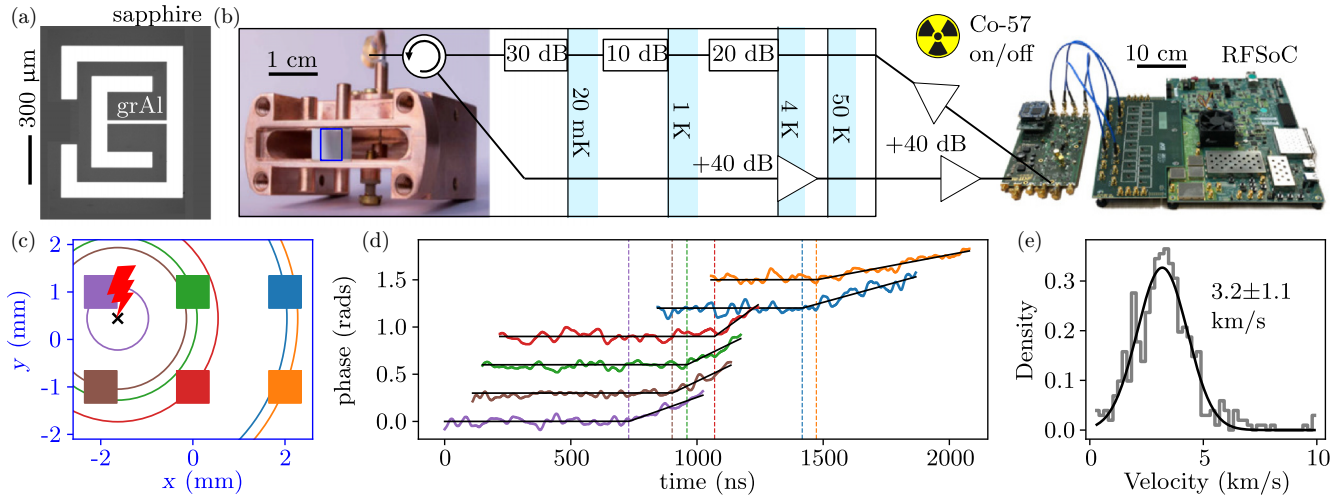

FIG. 1. Experimental setup. (a) micrograph of one of the six granular aluminum (grAl, white) superconducting resonators on a sapphire (gray) chip. The lumped design, inherited from Ref. [24], comprises an inductive wire, which acts as the absorber converting phonons to quasiparticles, while the width of the electrode pitch can be swept to change the resonator frequency. (b) schematics of cryostat and microwave wiring. The seismic array chip is glued into a copper waveguide mounted at the mixing chamber stage of a dilution cryostat. The signal is attenuated from room temperature at successive temperature stages, and recovered via low noise amplifiers at 4 K and at room temperature. The drive and readout electronics consist of a commercial Radio Frequency System-on-Chip (RFSoC) board with custom firmware for baseband signal generation, real-time frequency comb demodulation, and online data processing, along with a custom analog front-end board that converts between baseband and radio frequency using a superheterodyne mixer approach (cf. Appendix A for details). A cobalt-57 source (trefoil symbol) can be put next to the cryostat to raise the radioactivity levels for control experiments. (c) schematics of the superconducting seismic array, composed of a 3×2 grid of resonators [colored squares, roughly to scale, cf. (a)] spaced 2 mm apart on a sapphire chip [blue rectangle in (b)]. An ionizing impact (red bolt) generates a phonon wave front that propagates isotropically from the impact point (black cross) via a quasidiffusive process (see main text for details). The arrival of the wave front at each resonator (color-coded circles) can be used to reconstruct the impact position, as well as to infer the wave front propagation velocity. (d), phase of the complex frequency response of each resonator/seismometer, used to reconstruct the impact position as indicated in (c), and using the same color palette. Traces are offset in steps of 0.3 radians for clarity, increasing by order of arrival time (dashed vertical line). (e) histogram of reconstructed propagation velocity of the phonon wave front for all registered impacts reported in Fig. 2(a) in 0.1 km/s bins (gray), together with fit to a Gaussian distribution (black).

amount of energy coupled by phonons into the superconducting resonator as

$$\delta E = -\underbrace{\frac{4}{\alpha}\frac{\delta f_0}{f_0}}_{=\delta x_{\mathrm{QP}}} n_{\mathrm{CP}} \Delta_0 V, \tag{1}$$

where α is the kinetic inductance fraction, $\delta f_0/f_0$ is the relative resonant frequency shift, δx_{QP} is the fractional shift in quasiparticle density, n_{CP} is the Cooper pair density, Δ_0 is the superconducting gap, and V is the mode volume.

The energy of incoming radiation is in the keV-MeV range [3,17], orders of magnitude greater than the maximum allowed phonon energy (circa 0.1 eV for sapphire [18]). This results in frequent scattering and a so-called quasidiffusive process for phonon propagation: a "ball" of phonons expands isotropically at some fraction of the speed of sound [19]. This is the mechanism inducing correlated bursts and errors in superconducting devices on the same chip.

In the spirit of Ref. [5], we use the time differential of wave front arrival on each of the N resonators which detect a burst to reconstruct the impact position. We use `scipy`'s least-squares method [20] to solve the system of N equations

$$\begin{aligned} &(x - x_k)^2 + (y - y_k)^2 - (t_{1k} + t)^2 c^2 = 0, \\ &\text{with} \quad t = \sqrt{(x - x_1)^2 + (y - y_1)^2}/c, \end{aligned} \tag{2}$$

where x, y is the impact point, c is the propagation velocity, and x_k, y_k are the coordinates of the k-th resonator, where k denotes the arrival order (x_1, y_1 is the position of the first resonator reached by the wave front), and t_{1k} is the differential time of arrival between the first and k-th resonator (cf. Appendix B). The minimum number of resonators to solve the system is $N = 4$, given that we do not know the time of the original impact, and the propagation velocity is possibly a function of the unknown impact energy [15]—for $N > 4$ this is an overcomplete system.

Once the phonon wave front reaches the resonator, quasiparticles are generated on a time scale that is faster than all other relevant dynamics in the resonator. This is justified by the energy of the phonons being orders of magnitude larger than the superconducting spectral gap (order of THz) [18] and the electron-phonon interactions times being on the order of a nanosecond [21]. Furthermore, the relaxation back to unperturbed resonant frequency, due to quasiparticles recombining into Cooper pairs, is slower than all other relevant dynamics in the resonator, and can be as long as seconds [22]. This entails that we can treat the induced frequency shift as a step function in time. Upon an instantaneous burst, the complex microwave reflection or transmission coefficient of the resonator starts on a trajectory towards the new state of shifted resonant frequency, which can be considered a steady state compared to the fast burst dynamics. We resolve the initial phase slope

following a burst and use it as a proxy for the energy deposited into the resonator [cf. Eq. (1)]. As such, by concomitantly monitoring the microwave response of multiple resonators, we can resolve both the impact position and an estimation of the wave front energy at each detector site, thereby implementing an on-chip seismic array.

III. EXPERIMENTAL SETUP

We fabricated a chip with $N = 6$ superconducting resonators in a multiplexed readout scheme, each playing the role of a seismometer. For the superconducting film we employ granular aluminum (grAl), because we can tune its kinetic inductance during deposition by controlling the flow of oxygen [23] while preserving $\mathcal{O}(10^5)$ internal quality factors in the single photon regime [22] even for highly oxidized samples. Higher kinetic inductance results in detectors with better responsivity [cf. Eq. (1)]. The resonator design, inherited from Ref. [24] and shown in Fig. 1(a), consists of two electrode pads connected by a wire acting as the inductor. The pitch in the top electrode can be swept to change the resonant frequency, in the case of our devices spanning the $8.7 - 9\,\mathrm{GHz}$ range. The 55-nm film is patterned on top of c-plane 330 μm-thick sapphire with a single lift-off optical lithography step. We measure the room-temperature resistance using test stripes deposited on the wafer in the same evaporation step and use the Mattis-Bardeen formula [23] to infer a kinetic inductance $L_K = 150\mathrm{pH}/\square$. By calculating the geometric inductance L_G from design parameters [25] we estimate a kinetic inductance fraction $\alpha = L_K/(L_K + L_G) \approx 0.9$. Further parameters are reported in Appendix C.

A schematic of the experimental setup is shown in Fig. 1(b). The sapphire chip hosting the resonators is glued into a copper waveguide (same design as Ref. [24]) using a 1:1 mixture of epoxy resin and silver powder with a 4 μm mean particle size. The suspended chip couples to the TE10 mode of the waveguide. The waveguide cutoff is at 4.5 GHz, well below the resonator frequencies. The waveguide is attached to the mixing chamber plate of a dilution cryostat. The microwave lines in the cryostat are attenuated for a nominal total of 60 dB on the way in. The signal is routed to and from the waveguide by means of a circulator, and amplified on the way up by both a High Electron Mobility Transistor at the 4 K plate and a room-temperature amplifier. We can artificially raise the environmental radioactivity by putting a cobalt-57 source in the proximity of the cryostat.

We developed in-house printed circuit boards to perform intermediate frequency signal generation and to facilitate both upconversion to and downconversion from RF frequencies (see Appendix A and Ref. [26]). A Field Programmable Gate Array (FPGA) board generates a frequency comb signal of six tones, filling a bandwidth of circa 300 MHz. This is mixed up and down in the analog front-end with an on-board phase locked loop at 9.05 GHz, resulting in the lower sideband being sent to the cryostat. The analog-to-digital sampling rate is 1 GHz, and the signal is filtered by a moving average filter with a ∼20 ns window. The demodulated signal is rotated onto the in-phase axis. The real-time trigger, implemented in the FPGA fabric, is activated when the imaginary quadrature of the demodulated signal surpasses a value corresponding to a phase of 15° for all active resonators within a 10 μs window. Upon triggering, the FPGA stores 1024 samples of the time trace of both quadratures before the trigger.

IV. CHARACTERISTIC LENGTH

We show an example of a reconstructed impact in Fig. 1(c), and correlated phase shifts of the resonators in Fig. 1(d). We fit the initial part of the response to a piecewise function composed of a baseline followed by a linear rise. We measure a quasidiffusive propagation velocity of 3.2 ± 1.1 km/s [cf. Fig. 1(e)]. As a sanity check, we verify that the slopes of resonator responses scale consistently for impacts close to each other. The reconstruction of impact positions is based on the assumption of isotropic propagation, which we test in Appendix D. Note that resonators in this work are operated in the bifurcated regime. This is necessary to ensure a viable signal-to-noise ratio given the fast integration time of 20 ns (cf. Appendix A 1).

We summarize key elements suggesting a characteristic length in Fig. 2. In Fig. 2(a), we show a scatter plot of the reconstructed positions of the impacts measured over a ∼88 h window. The positions are reported as exact and uncertainties get encoded in the deviation of the propagation velocity. Note that the impact points all fit within the chip dimensions, despite no fitting boundaries being imposed on the x, y coordinates, confirming the quality of the position reconstruction method. Furthemore, note that the impacts seem to bunch around the centroid of the resonator grid, in contrast to the expected impact flux, which should be uniform over the whole chip [27]. We hypothesize that the phonon wave front disperses its energy as it travels across the chip, and with increasing distance it is increasingly likely that the energy deposited in the resonators is not sufficient to activate the trigger.

To further confirm this distance scaling, we report burst rates in Fig. 2(b) for different triggering protocols and environmental radioactivity conditions. We report histograms of the waiting time between bursts, showing the expected Poisson distribution, together with the exponential fit used to extract the burst rate. The rate of registered impacts increases fourfold when we relax the requirements to record a burst on triggering four neighboring resonators only. When we allow bursts to be recorded on triggering a single resonator, the measured burst rate further increases to ∼40 mHz (not depicted). Restricting the number of resonators that need to be triggered results in a smaller area of correlation. The observed increase in rate further seems to suggest the existence of a characteristic length comparable to the grid size. As a sanity check, we boost the naturally occurring radioactivity of the laboratory environment by adding a cobalt-57 source in the vicinity of the cryostat. This results in an increase in correlated burst rates when triggering on four and six resonators, and with the rate on four resonator triggering still being the largest one. In measurements with the source present, the impact rates triggering only four or all six resonators become closer to each other. This suggests that adding the radioactive source results in an increased number of higher energy impacts, i.e., proportionally more impacts have enough energy to result in long range correlation.

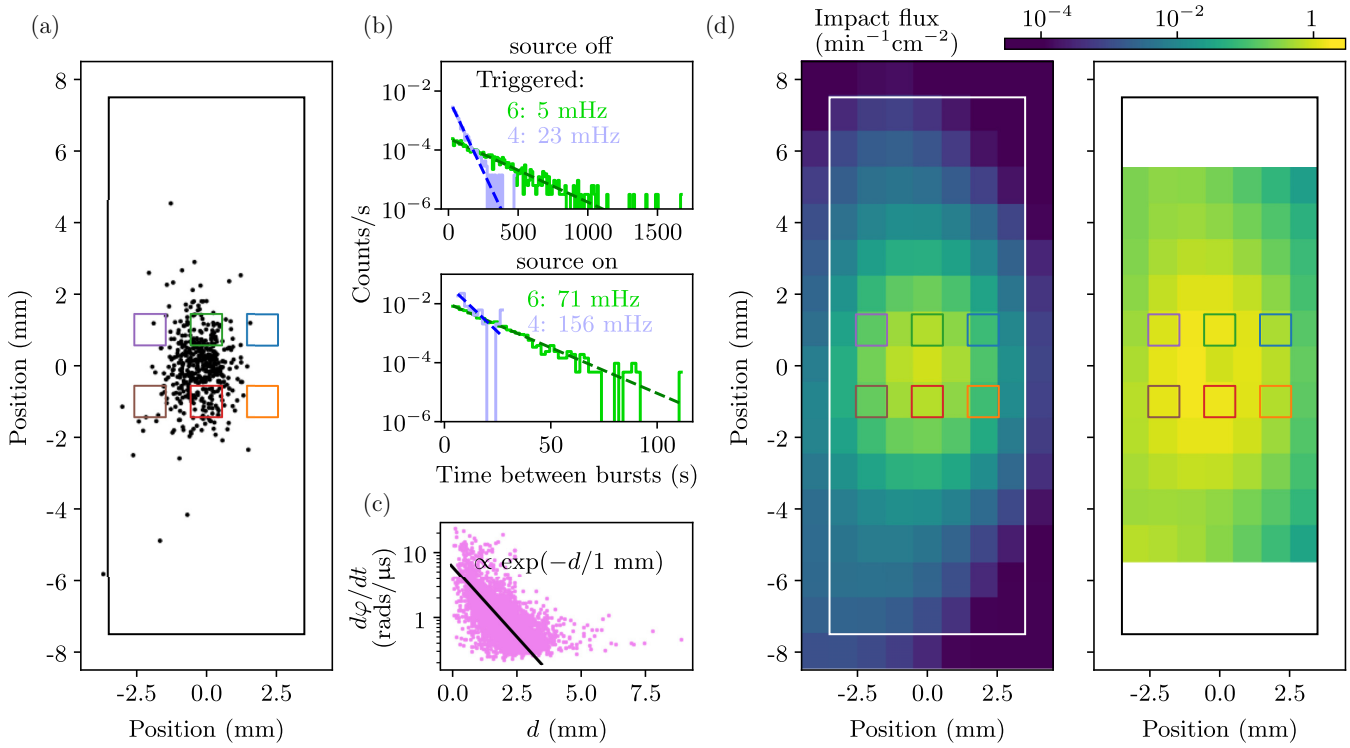

FIG. 2. Characteristic length. (a) scatter plot of reconstructed positions of impacts on the chip (black) over a ∼88 h measurement window. The chip boundaries are shown as an empty rectangle; resonators (roughly to scale) are shown as empty squares [cf. color palette of Figs. 1(c) and 1(d)]. (b) distributions of waiting times between successive bursts from environmental radiation (top) and with the addition of a radioactive source (bottom), with 10 s and 2 s binning, respectively. Impacts correlated across six (four) resonators are shown in green (blue) histograms. Exponential fits (solid lines) are used to extract the reported rates. All other panels in this figure report data measured without the source. (c) slope of the phase rise as a proxy for the energy deposited in the resonators by the reconstructed impacts, as a function of their distance from each resonator (pink), together with an exponential decay with 1 mm characteristic length (black). (d) reconstructed flux of ionizing particles impinging on the chip, reported both as-is (left) and after applying a scaling with the characteristic length of (c) (cf. main text for discussion). The color bar is shared across the two panels.

To assess quantitatively the characteristic length, in Fig. 2(c) we show the slope of the phase rise as a proxy for the energy absorbed by each resonator [cf. Eq. (1)] as a function of the distance between resonator and impact point, for all impacts reported in Fig. 2(a). The data suggest that the energy of phonons reaching the resonators decays over a millimetric length, comparable to Ref. [15]. To confirm that this is indeed the scaling visible in Fig. 2(a), we show a kernel density estimation of the measured impact flux on the chip in Fig. 2(d). This is obtained by summing normalized, symmetric Gaussians centered at the reconstructed impact positions [black markers in Fig. 2(a)] with a width that encodes the uncertainty on the propagation velocity. The Gaussian width is spanned by the two extremal distances obtained by recalculating the impact position using propagation velocities spanning a standard deviation about the mean [cf. Fig. 1(e)]. In the left panel we report the measured flux, showing the same spatial distribution of Fig. 2(a). In the right panel we show the same flux scaled by $\exp(-d/1\ \mathrm{mm})$, where d is the distance from the centroid of the resonator grid. For clarity, we only show it over the portion of the chip in which we actually measured impacts. This unbiased flux more closely resembles the expected one, with a uniform spatial distribution and a rate of a few impacts per minute per square centimeter [27]. We wish to stress that the exponential fit used here is a phenomenological tool to rescale the flux, with no underlying model. Developing a microscopic model for the decay mechanism is an outstanding task, albeit outside the scope of this work.

V. CONCLUSIONS

We reported measurements of correlated quasiparticle bursts from ionizing radiation in a superconducting quantum device made of six resonators in a multiplexed readout scheme. We reconstructed the position of the high-energy particle impacts on the chip, and inferred the propagation velocity of the generated athermal phonons. With these data at hand, we uncovered a characteristic length of the phonon mediated quasiparticle bursts on the order of 1 mm for the case of a bare sapphire substrate. Note that the reported length is comparable (to order of magnitude) to observations in superconducting quantum processors, e.g., Ref. [8] reports correlated errors saturating ∼15 qubits on a 26 qubit grid that is on the order of a squared centimeter. This suggests that, in larger (several cm^2) quantum processor chips, the correlated nature of most errors due to ionizing radiation will be confined to a subset of qubits within a few mm^2. It is important to

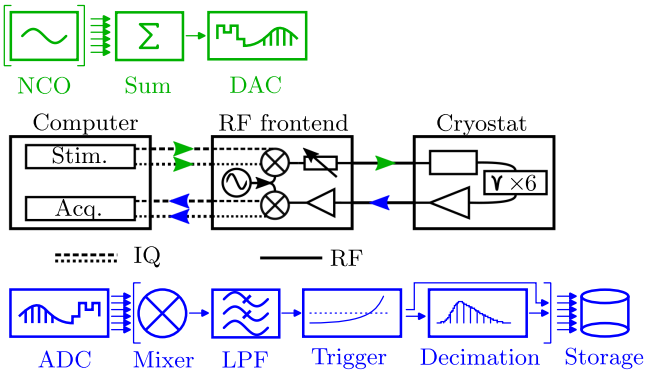

FIG. 3. Custom electronics. Block diagram of the custom electronics.

note that, for the sake of simplicity, our results were obtained on an empty substrate. Adding various metalization layers, as is the case in a quantum processor, could increase or decrease the correlation length resulting from this characteristic length, depending on the quasiparticle-phonon generation-recombination dynamics. Therefore, future research avenues include the quantification of the characteristic length and resulting correlation length of correlated qubit errors in actual quantum processors (similar to Refs. [7,28]), and measurements in the spirit of Ref. [15] dedicated to linking the propagation velocity to the phonon energy.

ACKNOWLEDGMENTS

We acknowledge P. Winkel, S. Geisert, N. Zapata, N. Gosling, and M. Field for fruitful discussion, and L. Radtke and S. Diewald for technical support. Facilities use is supported by the KIT Nanostructure Service Laboratory (NSL). We acknowledge funding from Google via their academic support initiative. F.V., P.P., T.R., and I.M.P. acknowledge support from the German Federal Ministry of Research, Technology and Space (BMFTR) within project GEQCOS (Grant No. FKZ: 13N15683). A.M. acknowledges support from the Alexander von Humboldt foundation in the framework of a Research Fellowship endowed by the German Federal Ministry of Education and Research.

The authors declare no competing interest.

DATA AVAILABILITY

The data that support the findings of this article are openly available [29].

APPENDIX A: CUSTOM ROOM-TEMPERATURE ELECTRONICS

The room-temperature electronics platform depicted on the right side of Fig. 1(b), and summarized in Fig. 3, is a superheterodyne setup divided in two stages. First, the baseband stage where the signal is generated using a AMD Xilinx RFSoC evaluation platform [30] and a custom designed signal fanout board (cf. Appendix A 1). The XCZU28 RFSoC device contains eight 6.5 GS s^{-1} digital-to-analog converters and eight 4 GS s^{-1} analog-to-digital converters (ADCs); both driven at 4 GS s^{-1}, with the data processing bandwidth set at 1 GS s^{-1}. Second, the Intermediate and Radio Frequency (RF) stage (cf. Appendix A 2) is provided by a custom high-frequency conversion and analog signal conditioning front-end board [26], providing vector signal generation and analysis. This setup can be used both for qubit characterization and quantum sensor measurement platforms [31,32].

1. Digital and baseband stage

The FPGA firmware generates a frequency division multiplexed comb containing six peaks through numerically controlled oscillators (one per resonator) at different resonant frequencies. The synthesis window has a total bandwidth of 1 GHz by means of two 500 MHz analog cables serving as an IQ interface. On the return path from the cryostat, the comb is mixed down to the baseband so that the ADCs can capture 1 GS s^{-1} of digital data. A set of digital mixers shifts the frequency of the signal from each resonator to DC. The demodulated voltage time series is passed through six (one per channel) independent 56-coefficient finite impulse response low-pass filters. This moving average window gives an effective sampling time of 20 nanoseconds. The filter coefficients were generated using the Python-based `scipy.signal` library and according to the `kaiser_beta` and `firwin` functions with the aforementioned 56 taps, nominal 10 MHz cutoff, and 60 dB of stop band rejection. A constant-phase offset calibration in the mixer rotates the demodulated signal onto the in-phase axis, such that the threshold trigger can work exclusively with the DC-like Q amplitude. Downsampling without aliasing can then be performed. Raw trigger data from a first-in-first-out array and subsequent points are then stored in 1024 sample windows, both at the net data rate and at a user-selectable subsampling rate (used to resolve the response of bursts with long tails). Stored values are then transferred to the RFSoC processor RAM and moved to the user PC via a custom software stack and the gRPC network framework [33].

When the demodulated imaginary quadrature of the voltage surpasses a user-controllable threshold, the channel is triggered. In this work, the trigger threshold was set individually for each channel to correspond to a 15° phase value. Upon triggering, the quadrature data (1024 nanosecond samples up to the trigger event) are saved to disk. Once triggered, the channel is locked to avoid new, potentially faulty triggers. The lock is released when fetching the data from the internal storage. A Python script on the analysis computer continuously checks the trigger status of the six channels simultaneously. When all channel triggers are activated from one cycle to the next, the event is recorded as a valid impact, and data is transferred to disk. Thus, the average cycle time, which is a few milliseconds, acts as a built-in cooldown period for the triggers. A further check that is performed to flag data as valid is that the timestamps of all triggers for a given impact must be within a 10 μs window to avoid triggering on longer relaxation tails (according to the spacing of the resonator grid and for a propagation velocity of 3 km/s, all bursts should happen within a 2 μs window).

2. Inter- and RF stage

The RF signal conditioning front-end contains aliasing filters for the ADC stages of the RFSoC, mixers for the frequency translation to the desired band, local oscillators to serve as their source, some amplification for substrate loss compensation, and variable attenuation. Everything is digitally controlled through serial interfaces and interpreted by a controller daughterboard for simple user interfacing through a Python-based Ethernet control stack.

A first stage IQ mixing translates between the dual 500 MHz baseband interface and the on-board interstage frequency of $2-4$ GHz. It consists of commercial wireless transceiver circuitry providing linearity and local oscillator isolation and filtering for harmonic rejection. The interstage signal is connected to the RF domain through mixers with single-ended connections. The RF side signal is band limited through a band-pass filter, the slope compensated through an equalization circuit, conversion and substrate losses compensated by amplifiers, and routed to SMA connectors. Variable attenuators are located on the transmission side of the RF stage and the reception side of the interstage frequency providing signal level adjustment.

Both mixing stages receive their local oscillator signals from on-board phase-locked loop (PLL) circuits which also incorporate voltage-controlled oscillators (VCO). Sweeping can be achieved through dynamic reconfiguration of either the PLL or by adjusting the baseband input signal on the FPGA. As the reference clock is shared for both PLLs, and mixing on all stages is performed with the same VCO source, the total additive phase noise contribution to the probe tones can be kept low through the provision of an external frequency reference.

The immediate bandwidth is given by the IQ interface, yielding 1 GHz. The RF bandwidth spans from 4 GHz to 10 GHz. The dynamic range of the attenuators is 31 dB, with spurious signals depending on the number of tones, desired output power, and frequency of the local oscillators.

APPENDIX B: POSITION RECONSTRUCTION

In order to determine the uncertainty of the position and velocity reconstructed from the impacts due to the finite time resolution, we simulate 10^4 impacts uniformly distributed on the chip, each generating a phonon wave front expanding with a velocity drawn from a normal distribution of 3 ± 1 km/s. The reconstructed position and velocity are well reconstructed in all cases. We simulate the effect of sampling time by recasting the continuous time variable as an integer number of 20 ns steps; the effective sampling time given by the width of the moving average filter (cf. Appendix A 1). In Fig. 4, we show that, even when accounting for the finite time resolution, positional errors are within 0.1 mm in the vicinity of the resonators (where all measured reconstructed impacts are registered), and velocity error is within 5% for all simulated impacts.

APPENDIX C: RESONATOR CHARACTERIZATION

We design our resonators to be spaced 50 MHz apart, by sweeping the electrode pitch [cf. Fig. 1(a)]. We validate

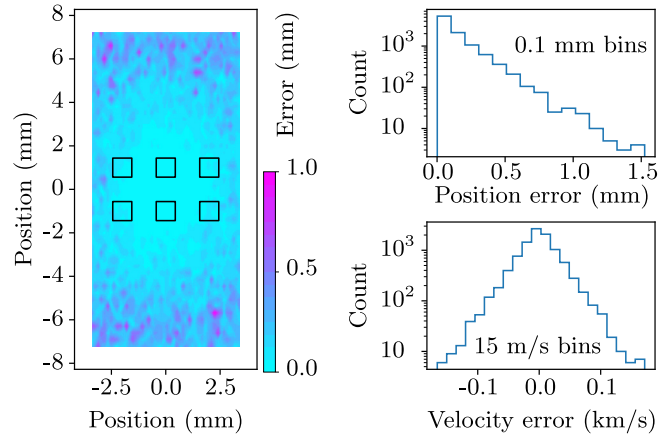

FIG. 4. Reconstruction error. Reconstructed position and velocity errors over 10^4 simulated impacts with a 20-ns time discretization.

the design by performing finite elements simulations using Ansyss HFSS. We characterize the resonators in frequency domain using a Keysight Vector Network Analyzer (VNA) to perform microwave reflection measurements, and by fitting the scattering parameters using Qkit [34], based on Ref. [35], allowing us to extract the resonant frequency as well as the internal and coupling quality factors. Extracted parameters are reported in Table I. The measured resonant frequencies are spaced 56 ± 6 MHz apart, in agreement with the designed ones. Note that the main measurement run took place 2/3 months after the VNA characterization, and as such we expect actual resonant frequencies to be on the order of 10–15 MHz lower due to oxidation aging since the chip was stored under ambient conditions [3].

We characterize nonlinear behavior by sweeping the probe power, and add the attenuation on the line down (circa 84 dB, measured with the cryostat open and constituted by 60 dB of nominal attenuation plus wiring and insertion loss) to obtain the power P_{cold} at the chip input. This, together with the resonator parameters, allows us to extract the average number of circulating photons using $\bar{n} = 4Q^2 P_{\mathrm{cold}}/(Q_c \hbar \omega_0^2)$. The resonant frequency of the resonators changes as a function of the readout photons due to the Kerr shift, resulting in a $K = 150 \pm 20$ mHz/photon shift across all resonators. This is in reasonable agreement with the *ab initio* value of 230 mHz/photon calculated using the grAl microscopic model from Ref. [36]. Furthermore, this allows us to estimate the critical number of photons at which bifurcation occurs as $n_c = \kappa/(2\pi\sqrt{3}K)$ [25,37]. The seismometry measurements are performed by operating the system in the deeply nonlinear regime (cf. rightmost two columns of Table I) in order to attain a viable signal-to-noise ratio despite the short integration times. We posit that this does not affect the fact that, for a small enough time after a burst, the phase rises linearly as in the case of resonator operated in the nonbifurcated regime [5,15]. Nevertheless, characterizing the nonlinear response to extract the value of energy deposited into the resonator is a valid research avenue for future development. Furthermore, one could employ a quantum limited amplifier to boost the signal, allowing resonators to be operated in the linear regime

TABLE I. Table of resonator parameters: resonant frequency f_0, internal and coupling quality factors Q_i and Q_c, resonator bandwidth $\kappa = f_0/Q$ where $Q^{-1} = Q_i^{-1} + Q_c^{-1}$, self-Kerr shift of the fundamental mode K, and critical and inferred average numbers of photons n_c and $\bar{n}$.

f_0 (GHz)	Q_i (10^5)	Q_c (10^5)	$\kappa/2\pi$ (kHz)	K (mHz/photon)	n_c (10^6)	$\bar{n}$ (10^6)
8.708	4.7	0.9	119	−133	0.5	10.1
8.772	5.7	0.9	116	−135	0.5	10.5
8.828	11.2	1.5	71	−116	0.4	17.8
8.883	4.4	0.4	242	−165	0.8	5.2
8.943	3.0	0.3	357	−195	1.1	3.5
8.989	2.0	0.6	194	−131	0.8	5.4

and Eq. (1) to be solved directly, thus reporting the actual energy absorbed in the resonator.

APPENDIX D: ISOTROPIC PROPAGATION

We wish to check whether the phonon wave front generated by impacts propagates with isotropic velocity. Reconstruction of the impact position is based on this assumption, so in the following we work with no knowledge of the position or time of the impact. The available data are the time differences of arrival (TDOAs) in the resonators. Under the assumption of an isotropic velocity c, the TDOA between two given resonators can range from 0 (if the impact is equidistant from them) to a maximum d/c, where d is the distance between the two resonators, in the case of the impact being on the outer portion of the line connecting the two resonators. Only in the latter configuration we get an unambiguous information about the propagation velocity along a given direction. The actual shape of the distribution of TDOAs bounded by these two extrema is nontrivially given by the geometry and size of the resonator grid and the chip. We are interested in the maxima of such distributions.

We extract the maxima of the TDOAs across nearest neighbor resonators in the vertical (three pairings), horizontal (four pairings), and diagonal (four pairings) directions by computing the mean and standard deviation of the 5% largest values in each set. We do this to obtain an estimate of the maximum that is more robust against glitches and undersampling. The resulting velocities are 3 ± 0.6, 2.9 ± 0.5, and 3.5 ± 0.5 km/s, respectively: within the error of this test, we can rule out major anisotropy within the symmetry of the square grid. By performing the same analysis for next-nearest neighbors (two horizontal steps, and two horizontal steps plus one vertical), we obtain 4.7 ± 0.5 and 4.7 ± 0.4 km/s, respectively: given the scarcity of events falling outside of the grid perimeter, we are less likely to sample impacts close to the outer line connecting resonators, and the resulting shorter TDOAs result in an inflated velocity. Further work in the spirit of Ref. [15] and using a grid of resonators could expand on this analysis in a more robust and quantitative way.

[1] T. Thorbeck, A. Eddins, I. Lauer, D. T. McClure, and M. Carroll, Two-level-system dynamics in a superconducting qubit due to background ionizing radiation, PRX Quantum **4**, 020356 (2023).

[2] A. P. Vepsäläinen, A. H. Karamlou, J. L. Orrell, A. S. Dogra, B. Loer, F. Vasconcelos, D. K. Kim, A. J. Melville, B. M. Niedzielski, and J. L. Yoder, Impact of ionizing radiation on superconducting qubit coherence, Nature (London) **584**, 551 (2020).

[3] L. Cardani, F. Valenti, N. Casali, G. Catelani, T. Charpentier, M. Clemenza, I. Colantoni, A. Cruciani, G. D'Imperio, L. Gironi, *et al.*, Reducing the impact of radioactivity on quantum circuits in a deep-underground facility, Nat. Commun. **12**, 2733 (2021).

[4] C. Larson, E. Yelton, K. Dodge, K. Okubo, J. Batarekh, V. Iaia, N. Kurinsky, and B. L. T. Plourde, Quasiparticle poisoning of superconducting qubits with active gamma irradiation, PRX Quantum **6**, 030339 (2025).

[5] L. J. Swenson, A. Cruciani, A. Benoit, M. Roesch, C. S. Yung, A. Bideaud, and A. Monfardini, High-speed phonon imaging using frequency-multiplexed kinetic inductance detectors, Appl. Phys. Lett. **96**, 263511 (2010).

[6] K. Karatsu, A. Endo, J. Bueno, P. J. de Visser, R. Barends, D. J. Thoen, V. Murugesan, N. Tomita, and J. J. A. Baselmans, Mitigation of cosmic ray effect on microwave kinetic inductance detector arrays, Appl. Phys. Lett. **114**, 032601 (2019).

[7] C. D. Wilen, S. Abdullah, N. A. Kurinsky, C. Stanford, L. Cardani, G. D'Imperio, C. Tomei, L. Faoro, L. B. Ioffe, C. H. Liu, *et al.*, Correlated charge noise and relaxation errors in superconducting qubits, Nature (London) **594**, 369 (2021).

[8] M. McEwen, L. Faoro, K. Arya, A. Dunsworth, T. Huang, S. Kim, B. Burkett, A. Fowler, F. Arute, J. C. Bardin, *et al.*, Resolving catastrophic error bursts from cosmic rays in large arrays of superconducting qubits, Nat. Phys. **18**, 107 (2022).

[9] E. Yelton, C. P. Larson, V. Iaia, K. Dodge, G. La Magna, P. G. Baity, I. V. Pechenezhskiy, R. McDermott, N. A. Kurinsky, G. Catelani, and B. L. T. Plourde, Modeling phonon-mediated quasiparticle poisoning in superconducting qubit arrays, Phys. Rev. B **110**, 024519 (2024).

[10] F. Henriques, F. Valenti, T. Charpentier, M. Lagoin, C. Gouriou, M. Martínez, L. Cardani, M. Vignati, L. Grünhaupt, D. Gusenkova, *et al.*, Phonon traps reduce the quasiparticle density in superconducting circuits, Appl. Phys. Lett. **115**, 212601 (2019).

[11] J. M. Martinis, Saving superconducting quantum processors from qubit decay and correlated errors generated by gamma and cosmic rays, npj Quantum Inf. **7**, 90 (2021).

[12] M. McEwen, K. C. Miao, J. Atalaya, A. Bilmes, A. Crook, J. Bovaird, J. M. Kreikebaum, N. Zobrist, E. Jeffrey, B. Ying, *et al.*, Resisting high-energy impact events through gap engineering in superconducting qubit arrays, Phys. Rev. Lett. **133**, 240601 (2024).

[13] E. Bertoldo, V. Pérez Sánchez, M. Martínez, M. Martínez, H. Khalife, and P. Forn-Díaz, Cosmic muon flux attenuation methods for superconducting qubit experiments, New J. Phys. **27**, 023014 (2025).

[14] R. Acharya, D. A. Abanin, L. Aghababaie-Beni, I. Aleiner, T. I. Andersen, M. Ansmann, F. Arute, K. Arya, A. Asfaw, N. Astrakhantsev, *et al.*, Quantum error correction below the surface code threshold, Nature (London) **638**, 920 (2025).

[15] G. Moshel, O. Rabinowitz, E. Blumenthal, and S. Hacohen-Gourgy, Propagation velocity measurements of substrate phonon bursts using MKIDs for superconducting circuits, Appl. Phys. Lett. **125**, 222601 (2024).

[16] P. K. Day, H. G. LeDuc, B. A. Mazin, A. Vayonakis, and J. Zmuidzinas, A broadband superconducting detector suitable for use in large arrays, Nature (London) **425**, 817 (2003).

[17] L. Cardani, I. Colantoni, A. Cruciani, F. De Dominicis, G. D'Imperio, M. Laubenstein, A. Mariani, L. Pagnanini, S. Pirro, C. Tomei, *et al.*, Disentangling the sources of ionizing radiation in superconducting qubits, Eur. Phys. J. C **83**, 94 (2023).

[18] Z. Cheng, Y. R. Koh, H. Ahmad, R. Hu, J. Shi, M. E. Liao, Y. Wang, T. Bai, R. Li, E. Lee, *et al.*, Thermal conductance across harmonic-matched epitaxial al-sapphire heterointerfaces, Commun. Phys. **3**115 (2020).

[19] R. W. Ogburn, A search for particle dark matter using cryogenic germanium and silicon detectors in the one- and two-tower runs of CDMS-II at Soudan, Ph.D. thesis, Stanford University, 2008, https://searchworks.stanford.edu/view/7860904.

[20] Scipy.optimize library, https://docs.scipy.org/doc/scipy/.

[21] S. B. Kaplan, C. C. Chi, D. N. Langenberg, J. J. Chang, S. Jafarey, and D. J. Scalapino, Quasiparticle and phonon lifetimes in superconductors, Phys. Rev. B **14**, 4854 (1976).

[22] L. Grünhaupt, N. Maleeva, S. T. Skacel, M. Calvo, F. Levy-Bertrand, A. V. Ustinov, H. Rotzinger, A. Monfardini, G. Catelani, and I. M. Pop, Loss mechanisms and quasiparticle dynamics in superconducting microwave resonators made of thin-film granular aluminum, Phys. Rev. Lett. **121**, 117001 (2018).

[23] H. Rotzinger, S. T. Skacel, M. Pfirrmann, J. N. Voss, J. Münzberg, S. Probst, P. Bushev, M. P. Weides, A. V. Ustinov, and J. E. Mooij, Aluminium-oxide wires for superconducting high kinetic inductance circuits, Supercond. Sci. Technol. **30**, 025002 (2017).

[24] P. Winkel, K. Borisov, L. Grünhaupt, D. Rieger, M. Spiecker, F. Valenti, A. V. Ustinov, W. Wernsdorfer, and I. M. Pop, Implementation of a transmon qubit using superconducting granular aluminum, Phys. Rev. X **10**, 031032 (2020).

[25] F. Valenti, F. Henriques, G. Catelani, N. Maleeva, L. Grünhaupt, U. von Lüpke, S. T. Skacel, P. Winkel, A. Bilmes, A. V. Ustinov, *et al.*, Interplay between kinetic inductance, nonlinearity, and quasiparticle dynamics in granular aluminum microwave kinetic inductance detectors, Phys. Rev. Appl. **11**, 054087 (2019).

[26] R. Gartmann, N. Karcher, R. Weller, O. Krömer, and O. Sander, Progress of the ECHo SDR readout hardware for multiplexed MMCs, J. Low Temp. Phys. **209**, 726 (2022).

[27] R. M. Barnett, C. D. Carone, D. E. Groom, T. G. Trippe, C. G. Wohl, B. Armstrong, P. S. Gee, G. S. Wagman, F. James, M. Mangano, *et al.*, Review of particle physics, Phys. Rev. D **54**, 1 (1996).

[28] R. Acharya, I. Aleiner, R. Allen, T. I. Andersen, M. Ansmann, F. Arute, K. Arya, A. Asfaw, J. Atalaya, R. Babbush, *et al.*, Suppressing quantum errors by scaling a surface code logical qubit, Nature (London) **614**, 676 (2023).

[29] F. Valenti, A. Murani, P. Paluch, R. Gartmann, L. Scheller, R. Weller, T. Reisinger, L. Ardila-Perez, and I. M. Pop, Data and code for: Seismometry of radiation-induced quasiparticle bursts in superconducting devices, Zenodo (2026), https://zenodo.org/records/19441411.

[30] Zynq UltraScale+ RFSoC ZCU111 Evaluation Kit, https://www.xilinx.com/products/boards-and-kits/zcu111.html.

[31] R. Gebauer, N. Karcher, D. Gusenkova, M. Spiecker, L. Grünhaupt, I. Takmakov, P. Winkel, L. Planat, N. Roch, W. Wernsdorfer, *et al.*, State preparation of a fluxonium qubit with feedback from a custom FPGA-based platform, in *Fifth International Conference on Quantum Technologies (ICQT-2019)* (AIP Publishing, Melville, 2020).

[32] M. E. G. Redondo, T. Muscheid, R. Gartmann, J. M. Salum, L. P. Ferreyro, N. A. Müller, J. D. Bonilla-Neira, J. M. Geria, J. J. Bonaparte, A. Almela, *et al.*, RFSoC Gen3-based software-defined radio characterization for the readout system of low-temperature bolometers, J. Low Temp. Phys. **215**, 161 (2024).

[33] N. Karcher, R. Gebauer, R. Bauknecht, R. Illichmann, and O. Sander, Versatile configuration and control framework for real-time data acquisition systems, IEEE Trans. Nucl. Sci. **68**, 1899 (2021).

[34] Qkit: a quantum measurement suite in Python, https://github.com/qkitgroup/qkit.

[35] S. Probst, F. B. Song, P. A. Bushev, A. V. Ustinov, and M. Weides, Efficient and robust analysis of complex scattering data under noise in microwave resonators, Rev. Sci. Instrum. **86**, 024706 (2015).

[36] N. Maleeva, L. Grünhaupt, T. Klein, F. Levy-Bertrand, O. Dupre, M. Calvo, F. Valenti, P. Winkel, F. Friedrich, W. Wernsdorfer, *et al.*, Circuit quantum electrodynamics of granular aluminum resonators, Nat. Commun. **9**, 3889 (2018).

[37] C. Eichler and A. Wallraff, Controlling the dynamic range of a Josephson parametric amplifier, EPJ Quantum Technol. **1**, 2 (2014).